ACCSCIENCE PUBLISHING

Materials Science in Additive Manufacturing

ORIGINAL RESEARCH ARTICLE

Powder spreading behavior of bimodal ceramics in the binder jetting process

Kazi Safowan Shahed[1], Willem Groeneveld-Meijer[2], Matthew Lear[3], Jeremy Schreiber[3], and Guha Manogharan[1,2]*

[1]Department of Industrial and Manufacturing Engineering, College of Engineering, The Pennsylvania State University, University Park, Pennsylvania, United States

[2]Department of Mechanical Engineering, College of Engineering, The Pennsylvania State University, City, Pennsylvania, United States

[3]The Applied Research Laboratory, The Pennsylvania State University, City, Pennsylvania, United States

Abstract

Binder jetting (BJT) has been extensively explored for additive manufacturing of ceramics due to its ability to create complex structures by processing refractory and hard-to-machine materials. However, achieving a uniform powder bed with high packing density while processing ceramics in BJT remains a challenge. This study systematically examines the role of powder size, powder temperature, flow behavior, and powder size distribution on powder bed formation and resulting part properties. Four different alumina powder sizes (1 μm, 5 μm, 10 μm, and 20 μm) were investigated. Flowability characterizations reveal that 1 μm powder remains poorly flowable at both room and elevated temperatures, while 20 μm powder demonstrates excellent flowability at both temperatures. Smaller powders, especially 1 μm, exhibit around 25% loss in moisture, which results in pronounced agglomeration at room temperature. Discrete element method simulations were used to identify the ideal mixing ratio of the bimodal powder using 5 μm and 20 μm powders. For bimodal powder, both the simulation and the experiments exhibited a preferential deposition of smaller powders in the spreading direction. However, the 5 μm and 20 μm powders did not show any preferential deposition in the simulation, but experiments showed preferential deposition behavior. When using bimodal powder, packing density decreases by 7.65% along the spreading direction, which aligns with an 8.19% drop in part relative density. These findings offer valuable insights into the effects of bimodal powder distribution for controlling powder bed packing density and potentially leveraging spatial density variations for functional applications such as biomedical implants, heat exchangers, and gas filtration.

Keywords: Additive manufacturing; Binder jetting; Bimodal powder; Ceramics; Powder bed density; Powder spreading

***Corresponding author:**
Guha Manogharan
(gum53@psu.edu)

Citation: Shahed KS, Groeneveld-Meijer W, Lear M, Schreiber J, Manogharan G. Powder spreading behavior of bimodal ceramics in the binder jetting process. *Mater Sci Add Manuf.* 2025;4(2):025110016. doi: 10.36922/MSAM025110016

Received: March 15, 2025

Revised: April 19, 2025

Accepted: April 28, 2025

Published Online: May 21, 2025

1. Introduction

Ceramics are highly versatile materials with a wide range of applications in biomedical implants, the casting industry, hypersonic devices, nuclear energy, energy storage devices, and catalytic converters. However, due to their brittle nature, ceramics are difficult to machine and impose design limitations when processed through conventional manufacturing processes.[1-4] With the advancements in additive manufacturing (AM), producing intricate shapes with ceramics is feasible and has garnered increased adoption. The binder jetting (BJT) process[5] is a non-phase transformation AM process that is particularly advantageous for refractory materials such as ceramics.[6,7] BJT is a powder bed process where a binder is selectively jetted on a layer of deposited powder based on slice information of part geometry to selectively bind the powders layer-by-layer, followed by curing of the binder and post-AM sintering.[7-9] Ceramic structures printed with BJT can have complex internal and external shapes[10-12] that are either infeasible or extremely difficult to manufacture by other conventional manufacturing processes.

In BJT manufacturing, the quality of the powder bed directly influences dimensional accuracy, surface finish, and final part density. Powder flowability is, therefore, an important factor, governing how uniformly powder can be deposited into successive layers during the printing process.[13] Flowability is dictated primarily by particle shape and size. Spherical particles offer reduced friction and interlocking during spreading, resulting in improved flow characteristics compared to irregularly shaped powders.[14-21] Similarly, coarse powders exhibit better flowability than fine powders due to weaker inter-particle cohesive forces. However, this improved spreadability comes at the cost of lower powder bed density, as larger particles inherently create more void space between them.[22,23] Despite ongoing efforts to balance the trade-off between flowability and packing efficiency,[24,25] robust strategies to consistently achieve both uniformity and high density in powder beds remain poorly understood, particularly for ceramic feedstocks, where cohesion, brittleness, and sensitivity to the environment exacerbates these challenges.

To address these competing requirements, bimodal powder systems, comprising a mixture of coarse and fine particles, have emerged as a promising approach. By enabling fine particles to occupy the interstitial voids between larger particles, bimodal distributions can increase the packing density while preserving acceptable flowability.[7,15,26] Clares *et al.*[7] reported a 20% improvement in green density and a 170% increase in flexural strength using a bimodal distribution compared to the best-performing unimodal powders. Bai *et al.*[26] further demonstrated that even when the median size remains constant, a broader particle size distribution (PSD) enhances bed density and improves part quality. Despite these advantages, bimodal powders are inherently prone to particle size segregation during spreading, where differences in size, mass, and cohesion lead to spatial variations in local packing density.[15,27] Such segregation may result in anisotropy in mechanical properties, dimensional variation, or print failure. However, the nature and implications of spatial segregation in bimodal ceramic powder beds remain inadequately characterized and are a central focus of this study.

The powder delivery system, including the feed system, the geometry, and the dynamics of the spreading mechanism, further influences the homogeneity and compaction of the powder bed. BJT systems typically utilize either an "in-layer feed" approach, where powder is moved laterally from a feedstock reservoir, or an "overhead feed" design, in which powder is dispensed vertically and leveled by a spreader.[28-32] In both configurations, the type of spreader, which is commonly either a blade or a roller, plays a pivotal role in shaping powder flow and deposition behavior.[33,34] Experimental and numerical studies have shown that roller spreaders outperform blades, promoting powder bed uniformity and reducing surface defects.[35,36] For instance, Lee *et al.*[37] used discrete element method (DEM) simulations to show that spreader speed influences particle segregation but lacked experimental validation. Moreover, many simulations predominantly focus on the heap formation in front of the recoater,[35,36,38] rather than the characteristics of the deposited layer itself. Oh *et al.*[39] reported uniform packing density in printed green parts but did not spatially resolve PSD within the bed. Other approaches, including binder pre-wetting and layer-by-layer compaction, have been investigated to improve homogeneity,[40,41] but these studies have primarily focused on unimodal powders. Thus, further investigation is required regarding how spreading systems interact with bimodal feedstocks to drive spatial variations in packing and microstructure.

While DEM simulations have advanced the understanding of powder spreading dynamics,[34,42,43] experimental validation of segregation phenomena for bimodal systems remains limited. Although counter-rotating roller configurations have been proposed to reduce segregation,[44-46] their effectiveness in controlling spatial heterogeneity in powder bed density has not been systematically demonstrated. Furthermore, the implications of such heterogeneity for printed part characteristics, particularly concerning density gradients and microstructural anisotropy, remain inadequately understood. These challenges become even more pronounced in the context of ceramic systems, where powders are composed of finer particle sizes, exhibit irregular morphologies, and demonstrate high susceptibility to cohesive forces and environmental moisture.[2,47-49] In contrast, metallic and polymeric powders typically benefit from gas atomization or controlled synthesis methods that yield uniform, spherical particles, thereby enhancing flowability and promoting greater uniformity in powder bed formation.[50,51] Although prior studies have established links between powder and process parameters and the resulting packing or part density in other material systems,[52-57] a comprehensive understanding of how spreading dynamics and feedstock characteristics interact to produce spatial variation in ceramic BJT remains lacking. This study addresses this gap by experimentally investigating the relationship between powder bed structure, segregation behavior, and resulting part density in bimodal ceramic systems.

This study presents an integrated numerical and experimental investigation of powder spreading behavior in BJT of bimodal alumina ceramics. This is the first work to spatially resolve variations in powder size distribution and packing density across the powder bed, revealing a consistent preferential deposition of finer particles at the leading edge of the spreading direction. We hypothesize that this phenomenon is driven by the reduced flowability of fine particles, attributed to stronger inter-particle cohesive forces, which leads to their early settlement and promotes differential powder packing. In addition, the flowability of the powders was analyzed, and laser diffraction analysis was employed to quantify segregation in unimodal and bimodal powders. The impact of these spatial powder characteristics was further assessed by correlating local bed packing density with the resulting relative density of printed parts. These findings offer new insights into the directional inhomogeneities introduced by powder spreading and underscore the need to consider spatial powder behavior in ceramic BJT processes.

2. Materials and methods

2.1. Powder characterization

Four different alumina (Al_2O_3) powders were obtained from Denka (Denka Chemicals GmbH, Japan) with 99% purity and size D(50) powder size distribution of 1 μm, 5 μm, 10 μm, and 20 μm. The 1 μm and 5 μm powders are considered fine powders, whereas the 10 μm and 20 μm powders are considered coarse powders. These powders fall within the usual powder size distribution used in the BJT.[58-61] The powders were analyzed with a Malvern Mastersizer 3,000 particle analyzer (Malvern Panalytical, United Kingdom). The apparent ($\rho_{apparent}$) density and tap (ρ_{tap}) density of the powders were measured using a graduated glass cylinder with a resolution of 0.1 mL and a digital weight scale with a resolution of 0.001 g. To understand the potential influence of residual heat on the powder bed, the apparent and tap densities were also measured at 120°C. These values were then used to compute the Hausner ratio (H) and Carr's index (C) as detailed in Equations I and II:

$$H = \frac{V_{apparent}}{V_{tap}} \tag{I}$$

$$C = \frac{\rho_{tap} - \rho_{apparent}}{\rho_{tap}} \tag{II}$$

Furthermore, the angle of repose was measured using a Hall Flowmeter funnel set up (Qualtech Products Industry, United States) for both the room-temperature powder and the heated powder. In addition, to understand the effect of the moisture in powder, a loss on ignition test was performed, where the powder was heated to 160°C for 5 min, and the loss in weight was recorded.[62]

2.2. Simulation setup

From the PSD analysis, 5 μm and 20 μm powders were selected for generating the bimodal powder to establish a bimodal powder with a fine and coarse powder. These powder sizes have been used in previous studies to create a bimodal powder.[61,63] While forming bimodal powder, the combination of fine powder with coarse powder allows for better flowability from the coarse powder and higher packing density, resulting in denser and stronger parts from the fine powder. An analytical model developed by Du *et al.*[3] was employed to determine the optimal mixing ratios for achieving higher packing density, given the known particle sizes. For a system containing two particle sizes, where D_1 is the diameter of the larger particles and D_2 is that of the smaller ones, the corresponding relationship is given by Equation III:

$$\varphi = min\ (\varphi_1, \varphi_2) \tag{III}$$

Here φ is the packing density for the bimodal mixture and is determined based on the packing density of the larger powder φ_1 and smaller powder φ_2 in the mixture. These individual packing densities are functions of several parameters, including ∂ (the separate packing density), F (volumetric fraction), $\tau_{1,2}$ (loosening effect), and $\epsilon_{1,2}$ (wall effect) corresponding to each particle size fraction. The effects of particle interactions, specifically the loosening effect ($\tau_{1,2}$) and the wall effect ($\epsilon_{1,2}$), are quantified using the following expressions as described in[64] in Equations IV and V:

$$\epsilon_{1,2} = 1 - \left(1 - \frac{D_2}{D_1}\right)^2 - \frac{0.4D_2}{D_1}\left(1 - \frac{D_2}{D_1}\right)^{3.7} \tag{IV}$$

$$\tau_{1,2} = 1 - \left(1 - \frac{D_2}{D_1}\right)^{3.3} - \frac{2.8D_2}{D_1}\left(1 - \frac{D_2}{D_1}\right)^{2.7} \qquad \text{(V)}$$

This study uses these equations to get the packing density of the bimodal powder used in the simulation of this study. The mixing ratios were analyzed based on the computational study by Shahed *et al.*,[6] and a volumetric ratio of 75%/25% was derived for 5 µm and 20 µm powders, resulting in a packing density of 0.71.

Discrete element modeling simulations were conducted using Flow3D (Flow Science Inc., United States) to generate representative powder beds with a mesh size of 0.22 mm. The DEM simulation was conducted using a cross-sectional representation of the actual system, measuring 4 cm × 1.625 cm, scaled down by a factor of four to reduce computational costs. A layer height of 50 µm was maintained throughout the simulation. To analyze particle distribution, sampling volumes were defined along two orientations: 4 cm × 0.1 cm × 0.005 cm in the spreading direction and 1.625 cm × 0.1 cm × 0.005 cm perpendicular to the spreading direction. These volumes were used to quantify the deposition of both large and small solid particles within the simulated domain. In addition, this powder settling simulation is representative of the overhang powder deposition system, as shown in Figure 1.

To ensure computational efficiency and tractability, the DEM simulations in this study involved several assumptions as used in previous studies.[34,36,46,65] All particles were modeled as discrete, rigid spheres to simplify contact interactions and reduce simulation complexity. As a result, any particle deformation during collisions was neglected. Moisture-related effects, such as capillary forces or humidity-induced agglomeration, were also not considered in the model, although they may influence powder behavior in experimental conditions. In addition, inter-particle interactions were represented using simplified force models that approximate cohesion and friction.

Following the settling simulation, a spreading simulation was performed to mimic the recoating process to generate the powder bed. A representative distribution of the bimodal powders (PSD that ranges from 2 µm, 4 µm, 5 µm, 10 µm, 15 µm, 18 µm, and 20 µm) was used to generate the powder bed (e.g., 2 µm, 4 µm, and 5 µm powders were used to represent the PSD of the 5 µm powder, and 10 µm, 15 µm, 18 µm, and 20 µm were used to represent the PSD of the 20 µm powder). As the spreading mechanism, a counter-rotating roller (0.4 cm diameter) was simulated with a traverse speed of 0.15 m/s at 250 rpm. The particles are defined as discrete rigid bodies, and the details of setting up the simulation can be found in Shahed *et al.*[6]. Three sampling volumes were set up in the *X*-axis (parallel to the spreading direction) at the beginning, middle, and end of the powder bed. Similarly, three sampling volumes were set up on the *Y*-axis (perpendicular to the spreading direction), as shown in Figure 2. The rationale for studying these multiple sampling volumes was to capture any variations in powder packing quality at different stages of the spreading cycle and across both the edges and center of the powder bed, thereby testing our hypothesis. From the count of the particles, the average size of particles in the sampling volume was calculated using the following Equation VI:

$$d_{avg} = \frac{\sum n_i . d_i}{\sum n_i} \qquad \text{(VI)}$$

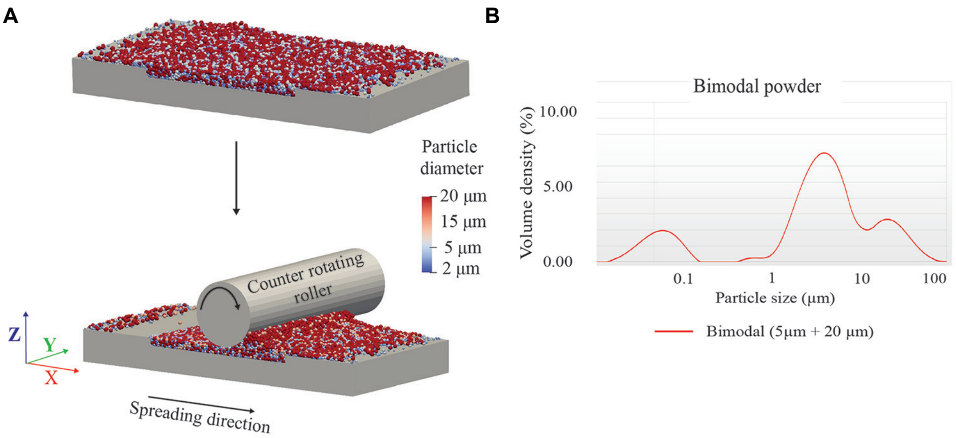

Figure 1. Discrete element method simulation workflow. (A) The powder settling simulation mimics the powder dropping from an overhead powder deposition system, followed by a powder spreading simulation with a counter-rotating roller. (B) Particle size distribution of the bimodal powder blend composed of 5 µm and 20 µm particles, demonstrating distinct peaks

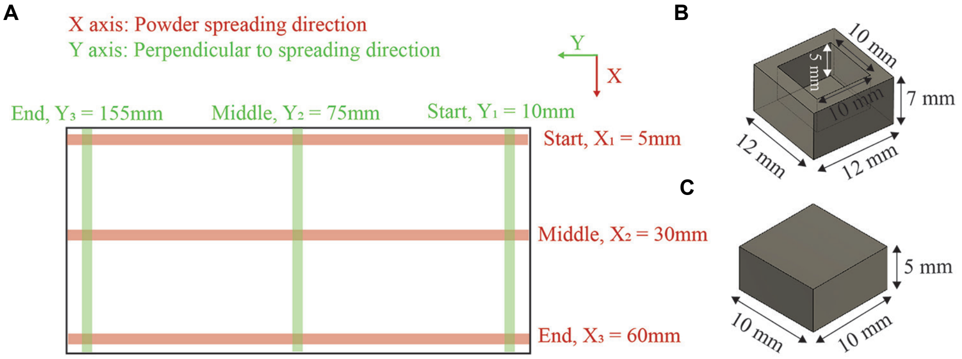

Figure 2. Location of sampling grid (A) Design of experiments ($n = 3$) to characterize powder sizes, powder bed packing densities, and part relative densities at X and Y locations of the powder bed. The dotted circle identifies the location of the density cups and the printed parts. (B) and (C) show the design and dimensions of the density cup and the part

where n_i and d_i are the total count and diameter of i^{th} type of powder. Furthermore, the packing density of the generated entire powder bed and the spatially varied six sampling volumes were extracted.

2.3. Powder formulation and spreading assessment

To test the powders under real printing conditions, all four powders were deposited in a commercially available ExOne Innovent+ (ExOne, United States) with a recoating speed of 10 mm/s and roller speed of 150 mm/s. The powders were spread at an elevated temperature to ensure successful powder bed generation. The bimodal powder was formulated by mixing 5 µm and 20 µm powders using a ball milling machine for two hours at 100 rpm based on findings from the simulation study.

2.4. Powder segregation assessment

Powder segregation analysis was conducted on 5 µm and 20 µm powders and the bimodal powder to see the effect of powders with different flowability. Following the generation of 50 layers with a layer height of 50 µm each, powders were collected using a plastic trough from three locations in the direction of the powder spreading (X-axis): start ($X_1 = 5$ mm), middle ($X_2 = 30$ mm), and end ($X_3 = 60$ mm). Similarly, another set of experiments was performed to collect the powders from three locations in the direction normal to the powder spreading (Y-axis): beginning ($Y_1 = 10$ mm), middle ($Y_2 = 75$ mm), and end ($Y_3 = 155$ mm). The PSDs of the collected powders were then analyzed using the Malvern Mastersizer 3,000 particle size analyzer. The experiments were repeated three times for statistical analysis.

2.5. Powder bed packing density

To measure the powder bed packing density, a modified density cup method[66] was used. The designed cup sizes were 12 mm × 12 mm × 7 mm with cavity dimensions of 10 mm × 10 mm × 5 mm. This resulted in a cup with a wall thickness of 2 mm and capable of capturing 100 layers of powder. These cups were strategically placed in nine different locations corresponding to the powder segregation assessment locations of the powder bed to get printed and capture the unprinted powder layers. The printing was performed on the same ExOne binder jet machine using their proprietary Fluidfuse binder at 100% binder saturation, binder set time of five seconds, and drying time of five seconds at 100% emitter output. After printing, the as-printed green parts were baked and cured for four hours at 180°C to impart handling strength to the cups. Subsequently, the density cups were carefully removed from the powder bed, and the powders were removed from the external walls of the cups with a brush. Following that, the mass of the cup was measured with the encased powder. After removing the encased powder from the cup, the packing density of the location of the cup was calculated based on Equation VII:

$$PD = \frac{m}{\rho \times V} \tag{VII}$$

where, m is the mass of the encased powder, ρ is the density of alumina, and V is the volume of the cavity in the density cup.

2.6. Printed samples

To understand the powder spreading effect on the printing process, a sample with dimensions of 10 mm × 10 mm × 5 mm was printed at distinct locations on the XY plane, similar to the density cups. The powder beds were generated using the identical spreading parameter described above, and identical printing and curing parameters were applied for three experiment repetitions ($n = 3$). Following the curing process, the samples were removed from the powder bed. A vernier caliper with a resolution of 0.001 mm was used to record the dimensions of the printed samples. The mass of the samples was measured on a scale with a resolution of 0.001 g. Based on the recorded dimensions and mass, and the theoretical density of the alumina, the relative density of the samples was calculated from Equation VIII:

$$\rho_R = \frac{\frac{m_s}{V}}{\rho_{alumina}} \qquad \text{(VIII)}$$

where ρ_R is the relative density, m_s is the mass of the sample, V is the volume of the sample, and $\rho_{alumina}$ is the theoretical density of alumina, which is 3.96 g/cm^3.

2.7. Statistical analysis

All statistical analyses were performed in Minitab (version 21.2, Minitab LLC, State College, PA, USA). Prior to hypothesis testing, the Shapiro-Wilk test ($\alpha = 0.05$) was applied to each data set to verify normality. When the normality assumption was held, group differences in powder size distribution, powder bed packing density, and green part relative density were evaluated with a one-way analysis of variance (ANOVA) conducted at a global two-sided significance level of $\alpha = 0.05$; effects were considered significant when $p<0.05$. If the data failed the normality check, group medians were compared with a Kruskal–Wallis one-way ANOVA on ranks to determine whether significant differences existed.

3. Results and discussion

3.1. Powder morphology and flowability

After analyzing the apparent density and tap density, the Hausner ratio and Carr's index of the unimodal powders were calculated. Furthermore, the angle of repose was measured for the powders. Figure 3 depicts all the values. Hausner ratio, Carr's index, and the angle of repose increased as the powder size and temperature decreased. Except for the 1 µm powder, all the other powders showed passable flowability at elevated temperatures in terms of the Hausner ratio as classified by Kaleem *et al.*[67] In addition, 1 µm powder has the lowest change in Hausner ratio due to temperature change while displaying poor flowability at both temperatures. This smaller change for 1 µm powder can be attributed to the agglomeration of the smaller powder, which then acts as a larger particle. On the contrary, the 20 µm powder exhibits excellent flowability at elevated and room temperatures. In addition, the

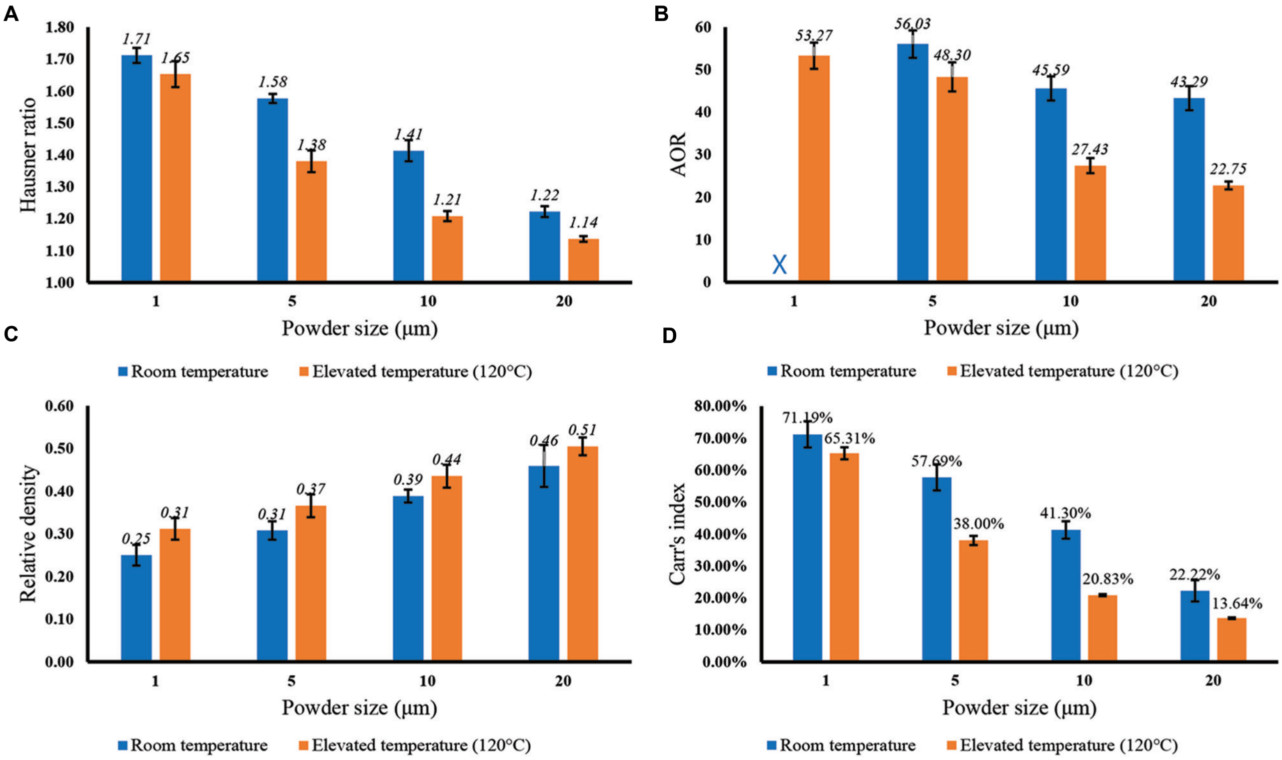

Figure 3. Different mechanical characteristics. (A) Hausner ratio, (B) angle of repose (AOR), (C) relative density, and (D) Carr's index, of alumina powders of varied sizes: 1 µm, 5 µm, 10 µm, and 20 µm. Note: X indicates the unsuccessful data collection of AOR for 1 µm powder at room temperature

10 μm powder shows the most significant improvement in flowability (17%) when exposed to elevated temperatures, with its flowability at elevated temperatures comparable to that of the 20 μm powder at room temperature. The elevated temperature generally improved the Hausner ratio for smaller powder, indicating better flowability.

Similarly, Carr's index for 1 μm and 5 μm powders indicates they have poor flowability,[67,68] which agrees with the Hausner ratio.[67,68] Except for the 1 μm powder, all the other powders showed notable changes in Carr's index, indicating the noteworthy influence of elevated temperature. While measuring the angle of repose (Figures 3B and 4), the 10 μm and 20 μm powders showed a dramatic increase (66.2% for 10 μm and 90.3% for 20 μm powder) in the angle of repose from the drop in powder temperature. On the other hand, 5 μm powder increased by around 16% when the temperature dropped to room temperature. Furthermore, the 1 μm powder did not even flow at room temperature. A close inspection showed high agglomeration in 1 μm powder, which hindered the flow.

In addition, the relative density was calculated for the powders, which showed that elevated temperature leads to higher relative density for all the powders. However, the smaller powders showed significant improvement in relative density, with the 1 μm showing a 25% increase with elevated temperature. While larger powder had higher relative density, 20 μm powder showed a large amount of variation at room temperature. Finally, a loss on ignition test revealed that the smaller size powders lost more moisture content compared to the larger powder, which indicates the presence of higher water content in the smaller powders. Moisture increases the cohesion between the powder particles, which can be attributed to higher agglomeration and poor flowability of the smaller powder size.[65,69] Overall, flowability and the deposition of smaller powders can be improved at elevated temperatures, resulting in better flowability and higher powder bed density.

3.2. Powder bed generation and powder segregation

The DEM simulation was performed following the study conducted by Shahed and Manogharan.[6] Six sampling volumes, three in representative x positions and three in representative y positions, were set up. The powder sizes and their count were recorded from these sampling volumes. Using Equation III, the average particle size, akin to D(50), was calculated for each of the sampling volumes. The simulation was performed for 5 μm, 20 μm, and bimodal powders. The simulations were repeated three times to capture the random generation of the particles and the spreading influence on the particles. For the 5 μm and 20 μm powders, the average particle size in both the spreading direction and the direction perpendicular to the spreading direction remains constant. One-way analysis of variance (ANOVA) at a significance level of 5% ($\alpha = 0.05$) revealed that there is no statistically significant variation ($p>0.75$) in either the spreading direction or the perpendicular to the spreading direction.

However, for the bimodal powder, the smaller particles were predominantly deposited at the beginning of the spreading process along the spreading direction, whereas larger particles accumulated toward the end. The results are shown in Figure 5. A one-way ANOVA at a significance level of 5% ($\alpha = 0.05$) showed that the variation in the average particle size is statistically significant ($p=0.001$) in the spreading direction. However, the variation in powder size perpendicular to the spreading direction was not statistically significant ($p=0.777$). This indicates that, for bimodal powders, the powder bed does not have a uniform powder size distribution, and there is a directionality in the change along the spreading directions. The results are shown in Figure 5A.

Following the simulations, spreading experiments on the machine were conducted for 5 μm, 20 μm, and bimodal powders to collect powder from the bed. The powders collected from different X locations (start, middle, and end) were analyzed for the PSD. The result showed a trend of depositing smaller particles at the beginning of the powder bed and larger particles at the end of the powder bed. This phenomenon was more prominent for the 20 μm powder than the 5 μm powder. The bimodal powder also showed a similar trend. Figure 5 shows the trend for D(50) of the powder size distribution. In addition, a one-way ANOVA was performed to see if the difference in powder

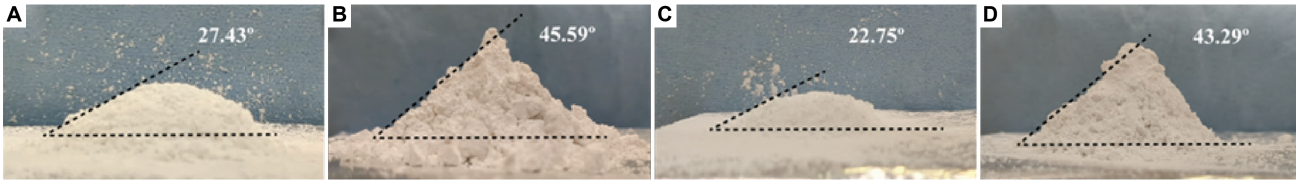

Figure 4. Change in angle of repose in 10 μm powder at (A) elevated temperature (120°C), (B) room temperature, and for 20 μm powder at (C) elevated temperature (120°C) and (D) room temperature

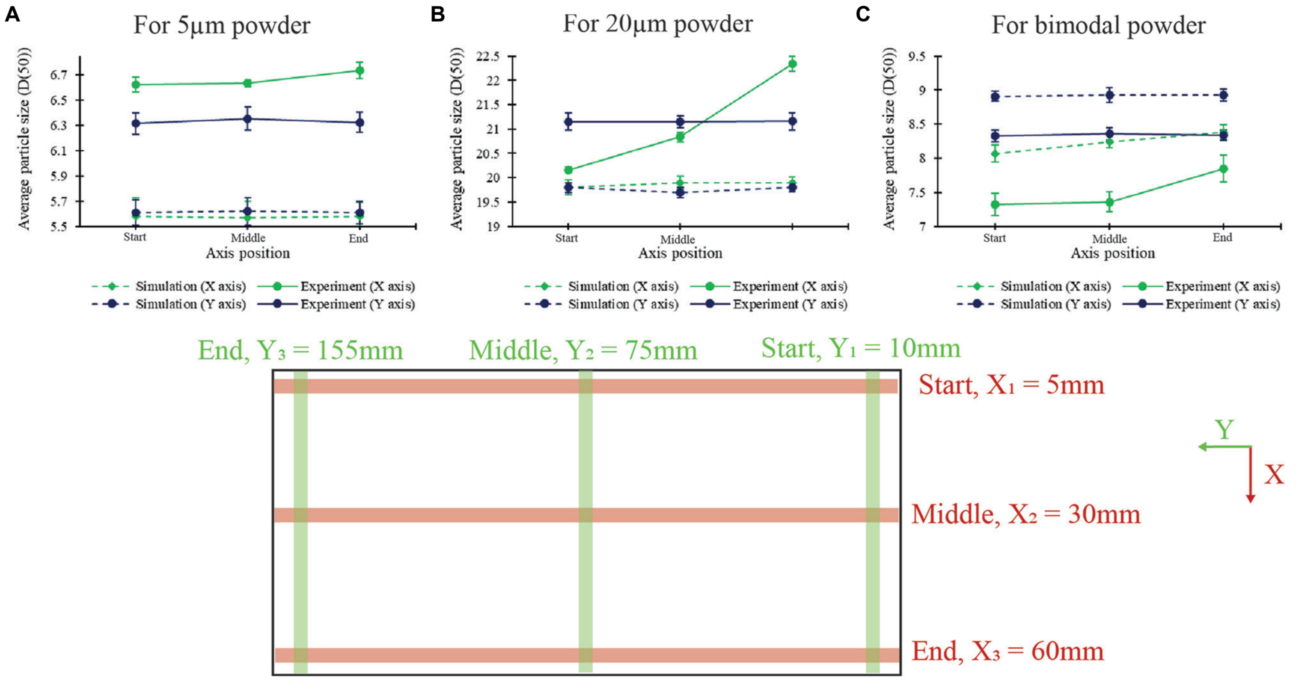

Figure 5. Comparison of simulated and experimental average particle sizes (D (50)) across different axis positions for (A) 5 μm powder, (B) 20 μm powder, and (C) bimodal powder blends. The bottom diagram illustrates the measurement grid used for sampling, showing the specific X-axis and Y-axis positions within the build platform

size was statistically significant. All the powders showed a statistically significant ($p<0.001$) difference in the powder size along the spreading direction. This confirms the preferential deposition of smaller powder at the beginning of the powder bed in the spreading direction. However, there was no statistically significant ($p>0.65$) difference in powder sizes perpendicular to the powder spreading direction for 5 µm, 20 µm, and bimodal powders.

For bimodal powder, the powder sizes in the experiments closely match the simulation. While both the simulation and experiments showed a preferential powder deposition in the spreading direction, the average particle size varied by 9.58% between the simulation (8.23 µm) and the experiment (7.51 µm). The variation was smaller, 6.41%, in the direction perpendicular to the spreading between the experiment (8.34 µm) and simulation (8.91 µm) average particle size. On the other hand, for both unimodal powders, the average powder size in the experiments deviated significantly from the simulation: 16.32% for 5 µm powder and 12.27% for 20 µm powder. The deviation between the simulated and experimentally measured particle sizes for unimodal powders arises primarily from the simplifying assumptions employed in DEM simulations. The simulation represents the PSD using a limited number of discrete particle sizes to approximate the unimodal distribution. Furthermore, the simulation treats particles as rigid, dry, perfectly spherical bodies, which do not fully represent the irregular shape of real ceramic powders, resulting in higher discrepancies between simulation and experiment. Finally, the preferential behavior of powder deposition in the direction of spreading, which can affect the packing density of the powder bed and final part density, was observed across all conditions.

The spatial variation in particle size observed along the powder spreading direction can be attributed to several particle-scale mechanisms inherent to granular flow dynamics. One major contributor is granular convection,[70] also referred to as the Brazil nut effect, where smaller particles tend to percolate downward, while larger particles migrate to the surface and are displaced toward the end of the spreading direction. This sorting can be exacerbated by the formation and collapse of the powder heap in front of the counter-rotating roller, where momentum differences between fine and coarse particles lead to differential settling. Wang *et al.*[36] described the inhomogeneity resulting from the powder bed using a roller from the powder burst phenomenon, which arises from the conflicting motion due to the rotation of the roller. In additon, van der Waals forces and moisture-induced cohesion play a significant role, particularly for finer alumina powders.[71,72] The loss on the ignition test confirmed that finer powders exhibit greater moisture retention, promoting cohesive clustering and reducing their flowability, which causes them to settle earlier in the spreading process. Furthermore, triboelectric charging from frictional contact with the spreader may create electrostatic forces that selectively hinder or enhance the transport of specific particle sizes.[73] These effects explain the preferential deposition of smaller particles at the beginning and larger particles toward the end of the spreading direction, as validated by simulation and experimental data.

3.3. Powder bed packing density

The packing density of the powder bed is an important aspect that influences the final quality of the final printed part. After the powder spreading simulation, the Flow-3D software (version 22.1.0.16, Flow Science, Santa Fe, NM, USA) was used to measure the packing density of the powder bed for the bimodal powder. To investigate the spatial packing density from random powder generation and spreading process, the packing density from all six sampling volumes was calculated along with the packing density of the total powder bed. The packing density for the start, middle, and end of the bed in the spreading direction was 0.7000, 0.6900, and 0.6800, respectively. The packing density perpendicular to the spreading direction was 0.6900 at all locations. Although there was a slight variation in packing density in the spreading direction, the variation was not observed perpendicular to the spreading direction. The average packing density of the powder bed was also 0.6900. This value shows a deviation of 1.45% from the packing density expected from the calculation of the powder fraction described in Section 2.2. This validates the powder fraction calculation. Furthermore, the packing density achieved in the simulation is within 10% of the previously reported studies.[74-76] The higher packing density can arise from the smaller powder size and the bimodal distribution of the powder size used in this study.

The packing density of the bimodal powder bed was measured using cups to capture the powder from distinct locations on the powder bed. The placement of the density cups, the mean, and the standard deviation of the measured packing density at each location are shown in Figure 6. A total of 27 measurements were taken, with each X and Y location having nine measurements. The average density of the powder bed was 0.6651, which is below 4% error compared to the simulation packing density of 0.6900. The average experimental packing density values are similar to those of the previous studies.[28,77] Previous studies have shown that smaller powder can increase the packing density of the powder bed.[78,79] The high experimental packing density can be attributed to the use of bimodal powder along with smaller particle sizes.

When looking at the spatial packing density, interesting patterns start to emerge. A statistical study was conducted

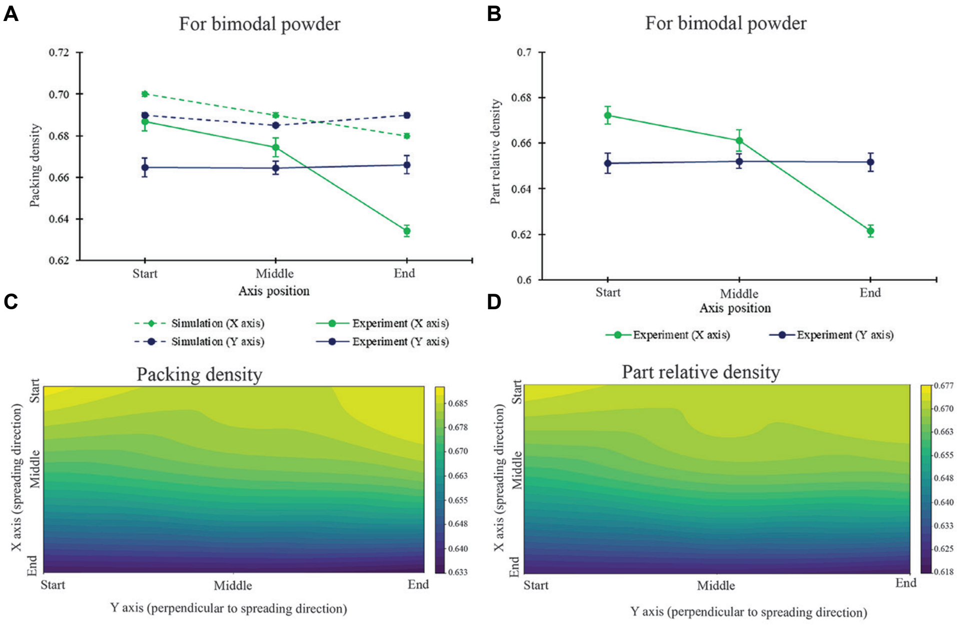

Figure 6. Packing density and part relative density from simulation and experiment for the bimodal powder (A) Comparison of simulated and experimental packing density of bimodal powder along the *X*- and *Y*-axes at different axis positions. (B) Experimental measurements of part relative density along the *X*- and *Y*-axes for bimodal powder at varying axis positions. The bottom schematic illustrates the build platform with designated measurement points (dotted circles) along the *X*-axis and *Y*-axis used for data collection. (C and D) show the contour plot for packing density and part relative density across the powder bed

to understand the variation from the measured packing density in the spreading direction. The difference in packing density was not statistically significant ($p>0.350$) within individual X positions; however, it was statistically significant ($p<0.001$) when comparing different X positions. There was a clear trend of packing density decreasing in the spreading direction. The average packing density at the beginning of the spreading process (X_1) was 0.6867, followed by 0.6745 in the middle (X_2), and 0.6342 at the end of the spreading process (X_3). The packing density decreases by 7.65% at the end of the spreading process compared to the beginning. However, the packing density remains relatively consistent along the perpendicular direction of the spreading for the given location in the spreading direction. The three separate locations sampled in the experiments yielded an average packing density of 0.6647, 0.6646, and 0.6661 at Y_1, Y_2, and $Y_{3,}$ respectively. These values are close to the overall average packing density of 0.6651. The sampling locations and the corresponding packing density measurements are shown in Figure 6.

From the experimental results, the packing density shows a decreasing trend in the spreading direction, which follows the trend of the preferential powder deposition discussed in the previous section. The smaller powders were deposited at the beginning of the spreading process, and the larger powders dominated at the end of the spreading process. The packing density was highest where the powder size distribution was dominated by smaller powder, which decreased with the increase in powder size. The reason is the smaller interparticle gap between smaller and larger powders. As the roller advances, regions increasingly dominated by coarser particles exhibit looser packing and reduced bulk density due to larger void spaces and reduced surface area for interparticle interactions. This gradient is further influenced by frictional resistance and shear-induced void during roller motion, which can temporarily expand the powder bed at certain locations, particularly where coarse particles dominate. However, in bimodal powder, the smaller particles help to reduce the interparticle gaps between the larger powder, resulting in increased packing density.[6,7] Increased packing density enhances binder penetration and reduces binder spreading time.[6] Furthermore, higher packing density enhances the green density, improving the final sintered density.[31] Similar directional density gradients and segregation-driven heterogeneities have also been reported in other ceramic systems, including titanium–aluminum alloys and alumina–zirconia composites, where powder bed and part characteristics were closely linked to initial packing structure.[58,80] It is possible to use the differential packing density in the same powder bed to impart different densities in the same part.

3.4. Part relative density

To understand the effect of the preferential powder deposition and density variation, a cube of 10 mm × 10 mm × 5 mm was printed at distinct locations on the *XY* plane, similar to the density coupons. The relative density of the green parts was calculated using Equation 5. As a result, the relative density followed the trend seen for the powder packing density. The relative density of the parts was higher at the beginning of the spreading direction and decreased from there. The average relative density of the printed samples measured at the start, middle, and end of the powder bed along the spreading direction is 0.6724, 0.6611, and 0.6215, respectively. This indicates a decrease in relative density at the end of the powder bed, amounting to 8.19% and 6.38% when compared to the start and middle of the bed, respectively. Similar to the packing density, there was no significant variation perpendicular to the spreading direction for a given X location. In addition, the average relative density measured perpendicular to the spreading direction exhibits negligible variation, with values of 0.6516 at location Y_1, 0.6521 at location Y_2, and 0.6512 at location Y_3. These values are close to the overall average packing density of 0.6517. The sampling locations and the corresponding relative density measurements are shown in Figure 6. The relative density of the printed parts lies within the range of the relative density observed for green parts with similar materials in previous studies.[32,77,81]

Compared to the packing density of the part, the relative density of the green parts decreased across all the samples, as shown in Figure 7. This can be attributed to the perturbation caused by the printing process. Binder kinetic energy, which is influenced by the velocity and size of the droplets, significantly affects the ejection of powder particles during the printing process.[82] The droplet in the BJT process can act as a projectile due to its kinetic energy, and when it impacts the powder bed, the momentum transfer can lead to local powder ejection or rearrangement. This effect is more pronounced at the end of the spreading direction, where packing density is already reduced due to preferential coarse particle deposition. In addition, the surface tension and spreading behavior of the binder can displace fine particles laterally or vertically, disturbing the initial packing achieved during spreading. Inkley *et al.*[40] showed that binder droplets can cause powder particles to be ejected from the bed, leading to increased porosity and reduced density in the final part. However, the binder introduces some mass in the green part from its own component. Although the solvent portion of the binder dries off during the curing process, it leaves behind the polymeric component, which helps to keep the shape intact. The difference between the powder bed packing density and the relative density indicates that

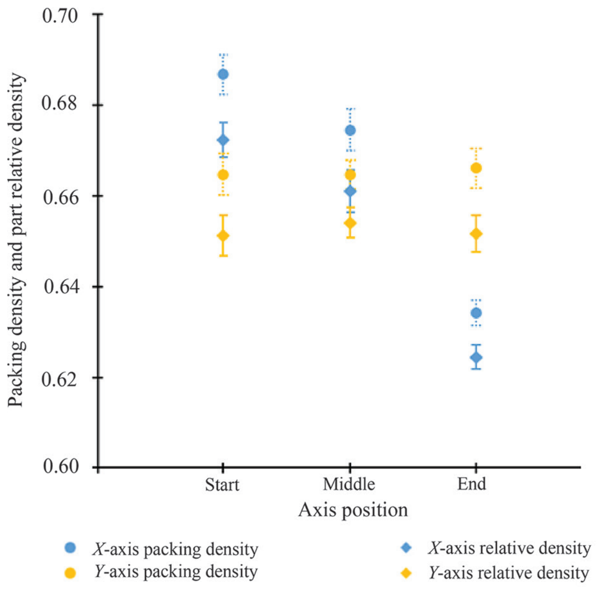

Figure 7. Comparison of packing density and part relative density along the *X*- and *Y*-axes at different axis positions. Packing density and part relative density along the *X*-axis show a decreasing trend in the spreading direction, indicating non-uniform powder spreading and part density

the amount of powder ejection was larger than the binder residue after curing. Previous studies also showed that smaller powders lead to higher green density.[7,81,82]

These results demonstrate that PSD directly affects the green part properties. Finer particles contribute to higher local packing density and, thus, yield higher relative density in the printed part, while coarser regions exhibit lower density. This spatial variation can be strategically used to design parts with location-specific properties. This graded density can potentially optimize mechanical properties, for instance, densifying certain regions for superior strength while maintaining lower density in others for lightweight design or thermal management.

4. Conclusion

AM processing physics in powder bed processes like BJT are readily affected by the powder bed spreading process and characteristics. This study systematically investigated the flowability of unimodal alumina powders (1 µm, 5 µm, 10 µm, and 20 µm) to choose a bimodal powder that shows the highest packing density. The 5 µm and 20 µm powders with a 4:1 volume-to-percentage ratio were chosen based on the DEM simulation to formulate the bimodal powder. This bimodal powder was used for further powder bed formation and printing experiments. Powder samples were collected from a powder bed deposited in a BJT machine that uses an overhead feed system and a roller-based powder spreading mechanism, where all the spreading and printing parameters were kept constant to isolate the effect of powder properties themselves. Subsequently, the powder bed density was measured using a density cup, and the relative density of the green parts was evaluated based on the printed samples. Some of the major findings from this study are given below:

(i) Smaller powders (1 µm and 5 µm) exhibited markedly improved flow characteristics when used at elevated temperatures, reducing moisture-induced agglomeration. On the other hand, coarser powders (10 µm and 20 µm) displayed excellent flowability across both room and higher temperatures.
(ii) Discrete element simulations and experiments revealed that, for the bimodal powder (5 µm and 20 µm), finer particles settled at the start of the spreading direction. In comparison, larger particles migrated toward the trailing edge, inducing a spatial gradient in powder size distribution.
(iii) The powder bed packing density also dropped in the spreading direction. Particularly, regions dominated by smaller particles showed denser packing, whereas the larger particle-dominated regions showed lower packing density, resulting in a packing density gradient along the spreading direction.
(iv) Local fluctuations in powder bed packing density were reflected in spatial variations of green part density, mirroring the same pattern of packing density observed in the powder bed.

These findings highlight the critical influence of PSD, temperature, flow behavior, and powder spreading behavior on powder bed uniformity, packing density, and green part density. The observed preferential deposition of smaller powders, coupled with differential packing densities, signifies the importance of addressing spatial inhomogeneities in powder bed-based AM. Furthermore, this phenomenon opens up the possibility of fabricating parts with functionally graded densities.

Acknowledgments

The authors would like to acknowledge Denka Chemicals GmbH, Tokyo, Japan, for their support in supplying all the powders used in this study.

Funding

This work was partially supported by NSF CMMI Award #1944120 and partially funded by Applied Research Laboratory, Penn State, through the Walker Student Fellowship.

Conflict of interest

Guha Manogharan serves as the Editorial Board Member of the journal, but was not in any way involved in the editorial and peer-review process conducted for this paper, directly or indirectly. Other authors declare they have no competing interests.

Author contributions

Conceptualization: Kazi Safowan Shahed, Guha Manogharan
Formal analysis: Kazi Safowan Shahed, Guha Manogharan
Funding Acquisition: Matthew Lear, Jeremy Schreiber, Guha Manogharan
Investigation: Kazi Safowan Shahed, Willem Groeneveld–Meijer
Methodology: Kazi Safowan Shahed, Willem Groeneveld–Meijer, Guha Manogharan
Writing – original draft: Kazi Safowan Shahed, Guha Manogharan
Writing – review & editing: Matthew Lear, Jeremy Schreiber, Guha Manogharan

Ethics approval and consent to participate

Not applicable

Consent for publication

Not applicable

Availability of data

Data will be made available on reasonable request.

References

1. Lv X, Ye F, Cheng L, Fan S, Liu Y. Binder jetting of ceramics: Powders, binders, printing parameters, equipment, and post-treatment. *Ceram Int*. 2019;45(10):12609-12624.

   doi: 10.1016/J.CERAMINT.2019.04.012

2. Zocca A, Colombo P, Gomes CM, Günster J. Additive manufacturing of ceramics: Issues, potentialities, and opportunities. *J Am Ceram Soc*. 2015;98(7):1983-2001.

   doi: 10.1111/JACE.13700

3. Du W, Singh M, Singh D. Binder jetting additive manufacturing of silicon carbide ceramics: Development of bimodal powder feedstocks by modeling and experimental methods. *Ceram Int*. 2020;46(12):19701-19707.

   doi: 10.1016/J.CERAMINT.2020.04.098

4. Jodati H, Yılmaz B, Evis Z. A review of bioceramic porous scaffolds for hard tissue applications: Effects of structural features. *Ceram Int*. 2020;46(10):15725-15739.

   doi: 10.1016/j.ceramint.2020.03.192

5. ISO/ASTM 52900:2015(en), *Additive Manufacturing-General Principles-Terminology*. Available from: https://www.iso.org/obp/ui/#iso: std:iso-astm:52900:ed-1:v1:en [Last accessed on 2025 Feb 07].

6. Shahed KS, Manogharan G. Powder-binder interaction in binder jetting process: A simulation study on bimodal powders. In: *Additive Manufacturing; Advanced Materials Manufacturing; Biomanufacturing; Life Cycle Engineering*. Vol. 1. New York City: American Society of Mechanical Engineers; 2023.

   doi: 10.1115/MSEC2023-104366

7. Clares AP, Gao Y, Stebbins R, Van Duin ACT, Manogharan G. Increasing density and mechanical performance of binder jetting processing through bimodal particle size distribution. *Mater Sci Addit Manuf*. 2022;1(3):20.

   doi: 10.18063/msam.v1i3.20

8. Shrestha S, Manogharan G. Optimization of binder jetting using taguchi method. *JOM*. 2017;69(3):491-497.

   doi: 10.1007/S11837-016-2231-4/TABLES/4

9. Mostafaei A, Elliott AM, Barnes JE, *et al*. Binder jet 3D printing-Process parameters, materials, properties, modeling, and challenges. *Prog Mater Sci*. 2021;119:100707.

   doi: 10.1016/J.PMATSCI.2020.100707

10. Sarila V, Koneru HP, Pyatla S, Cheepu M, Kantumunchu VC, Ramachandran D. An overview on 3D printing of ceramics using binder jetting process. *Eng Proc*. 2024;61(1):44.

    doi: 10.3390/ENGPROC2024061044

11. Huang S, Ye C, Zhao H, Fan Z. Additive manufacturing of thin alumina ceramic cores using binder-jetting. *Addit Manuf*. 2019;29:100802.

    doi: 10.1016/J.ADDMA.2019.100802

12. Du W, Ren X, Pei Z, Ma C. Ceramic binder jetting additive manufacturing: A literature review on density. *J Manuf Sci Eng Trans ASME*. 2020;142(4):1074276.

    doi: 10.1115/1.4046248/1074276

13. Clares AP, Manogharan G. Discrete-element simulation of powder spreading process in binder jetting, and the effects of powder size. In: *Proceedings of the ASME 2021 16th International Manufacturing Science and Engineering Conference, MSEC 2021*; 2021. p. 1.

    doi: 10.1115/MSEC2021-63351

14. Zegzulka J, Gelnar D, Jezerska L, Prokes R, Rozbroj J. Characterization and flowability methods for metal powders. *Sci Rep*. 2020;10(1):21004.

    doi: 10.1038/s41598-020-77974-3

15. Haferkamp L, Haudenschild L, Spierings A, *et al*. The influence of particle shape, powder flowability, and powder layer density on part density in laser powder bed fusion. *Metals (Basel)*. 2021;11(3):418.

    doi: 10.3390/met11030418

16. Garboczi EJ, Hrabe N. Particle shape and size analysis for

metal powders used for additive manufacturing: Technique description and application to two gas-atomized and plasma-atomized Ti64 powders. *Addit Manuf*. 2020;31:100965.

doi: 10.1016/j.addma.2019.100965

17. Mussatto A, Groarke R, O'Neill A, Obeidi MA, Delaure Y, Brabazon D. Influences of powder morphology and spreading parameters on the powder bed topography uniformity in powder bed fusion metal additive manufacturing. *Addit Manuf*. 2021;38:101807.

    doi: 10.1016/j.addma.2020.101807

18. Yim S, Bian H, Aoyagi K, Yamanaka K, Chiba A. Effect of powder morphology on flowability and spreading behavior in powder bed fusion additive manufacturing process: A particle-scale modeling study. *Addit Manuf*. 2023;72:103612.

    doi: 10.1016/j.addma.2023.103612

19. Anderson IE, White EMH, Dehoff R. Feedstock powder processing research needs for additive manufacturing development. *Curr Opin Solid State Mater Sci*. 2018;22(1):8-15.

    doi: 10.1016/j.cossms.2018.01.002

20. Freeman R. Measuring the flow properties of consolidated, conditioned and aerated powders -A comparative study using a powder rheometer and a rotational shear cell. *Powder Technol*. 2007;174(1-2):25-33.

    doi: 10.1016/j.powtec.2006.10.016

21. Chan LCY, Page NW. Particle fractal and load effects on internal friction in powders. *Powder Technol*. 1997;90(3): 259-266.

    doi: 10.1016/S0032-5910(96)03228-7

22. Jange CG, Ambrose RPK. Effect of surface compositional difference on powder flow properties. *Powder Technol*. 2019;344:363-372.

    doi: 10.1016/j.powtec.2018.12.027

23. Qu Z, Zhang P, Lai Y, Wang Q, Song J, Liang S. Influence of powder particle size on the microstructure of a hot isostatically pressed superalloy. *J Mater Res Technol*. 2022;16:1283-1292.

    doi: 10.1016/j.jmrt.2021.12.081

24. Diener S, Zocca A, Günster J. Literature review: Methods for achieving high powder bed densities in ceramic powder bed based additive manufacturing. *Open Ceram*. 2021;8:100191.

    doi: 10.1016/J.OCERAM.2021.100191

25. Wang J, Jeong SG, Kim ES, Kim HS, Lee BJ. Material-agnostic machine learning approach enables high relative density in powder bed fusion products. *Nat Commun*. 2023;14(1):1-12.

    doi: 10.1038/s41467-023-42319-x

26. Bai Y, Wagner G, Williams CB. Effect of bimodal powder mixture on powder packing density and sintered density in binder jetting of metals. In: *International Solid Freeform Fabrication Symposium*. University of Texas at Austin; 2015. Available from: https://repositories.lib.utexas.edu/handle/2152/89376 [Last accessed on 2022 Oct 19].

27. Yao D, Wang J, Li M, *et al*. Segregation of 316L stainless steel powder during spreading in selective laser melting based additive manufacturing. *Powder Technol*. 2022;397:117096.

    doi: 10.1016/J.POWTEC.2021.117096

28. Moghadasi M, Miao G, Li M, Pei Z, Ma C. Combining powder bed compaction and nanopowders to improve density in ceramic binder jetting additive manufacturing. *Ceram Int*. 2021;47(24):35348-35355.

    doi: 10.1016/J.CERAMINT.2021.09.077

29. Miao G, Moghadasi M, Du W, Pei Z, Ma C. Experimental investigation on the effect of roller traverse and rotation speeds on ceramic binder jetting additive manufacturing. *J Manuf Process*. 2022;79:887-894.

    doi: 10.1016/J.JMAPRO.2022.05.039

30. Li M, Wei X, Pei Z, Ma C. Binder jetting additive manufacturing: Observations of compaction-induced powder bed surface defects. *Manuf Lett*. 2021;28:50-53.

    doi: 10.1016/j.mfglet.2021.04.003

31. Porter Q, Li M, Pei Z, Ma C. Binder jetting additive manufacturing: The effect of feed region density on resultant densities. *J Manuf Sci Eng*. 2022;144(9):1140557.

    doi: 10.1115/1.4054453/1140557

32. Li M, Miao G, Moghadasi M, Pei Z, Ma C. Ceramic binder jetting additive manufacturing: Relationships among powder properties, feed region density, and powder bed density. *Ceram Int*. 2021;47(17):25147-25151.

    doi: 10.1016/j.ceramint.2021.05.175

33. Chen H, Chen Y, Liu Y, Wei Q, Shi Y, Yan W. Packing quality of powder layer during counter-rolling-type powder spreading process in additive manufacturing. *Int J Mach Tools Manuf*. 2020;153:103553.

    doi: 10.1016/J.IJMACHTOOLS.2020.103553

34. Haeri S. Optimisation of blade type spreaders for powder bed preparation in Additive Manufacturing using DEM simulations. *Powder Technol*. 2017;321:94-104.

    doi: 10.1016/J.POWTEC.2017.08.011

35. Haeri S, Wang Y, Ghita O, Sun J. Discrete element simulation and experimental study of powder spreading process in additive manufacturing. *Powder Technol*. 2017;306:45-54.

    doi: 10.1016/J.POWTEC.2016.11.002

36. Wang L, Yu A, Li E, Shen H, Zhou Z. Effects of spreader geometry on powder spreading process in powder bed additive manufacturing. *Powder Technol*. 2021;384:211-222.

    doi: 10.1016/J.POWTEC.2021.02.022

37. Lee Y, Nandwana P, Simunovic S. Powder spreading, densification, and part deformation in binder jetting additive manufacturing. *Prog Addit Manuf*. 2022;7(1):111-125.

    doi: 10.1007/S40964-021-00214-1/FIGURES/13

38. Chen H, Wei Q, Wen S, Li Z, Shi Y. Flow behavior of powder particles in layering process of selective laser melting: Numerical modeling and experimental verification based on discrete element method. *Int J Mach Tools Manuf*. 2017;123:146-159.

    doi: 10.1016/J.IJMACHTOOLS.2017.08.004

39. Oh JW, Nahm S, Kim B, Choi H. Anisotropy in green body bending strength due to additive direction in the binder-jetting additive manufacturing process. *J Korean Instit Metals Mater*. 2019;57(4):227-235.

    doi: 10.3365/KJMM.2019.57.4.227

40. Inkley CG, Lawrence JE, Crane NB. Impact of controlled prewetting on part formation in binder jet additive manufacturing. *Addit Manuf*. 2023;72:103619.

    doi: 10.1016/J.ADDMA.2023.103619

41. Inkley C, Martin D, Clark B, Crane N. Controlled Wetting of Spread Powder and its Impact on Line Formation in Binder Jetting. In: *Proceedings of ASME 2022 17th International Manufacturing Science and Engineering Conference, MSEC 2022*; 2022. p. 1.

    doi: 10.1115/MSEC2022-85603

42. Nan W, Pasha M, Ghadiri M. Numerical simulation of particle flow and segregation during roller spreading process in additive manufacturing. *Powder Technol*. 2020;364:811-821.

    doi: 10.1016/J.POWTEC.2019.12.023

43. Phua A, Doblin C, Owen P, Davies CHJ, Delaney GW. The effect of recoater geometry and speed on granular convection and size segregation in powder bed fusion. *Powder Technol*. 2021;394:632-644.

    doi: 10.1016/J.POWTEC.2021.08.058

44. Miao G, Du W, Pei Z, Ma C. A literature review on powder spreading in additive manufacturing. *Addit Manuf*. 2022;58:103029.

    doi: 10.1016/J.ADDMA.2022.103029

45. Bierwisch C. *DEM Powder Spreading and SPH Powder Melting Models for Additive Manufacturing Process Simulations*; 2019. Available from: https://publica.fraunhofer.de/handle/publica/406662 [Last accessed on 2025 Jan 29].

46. Haeria S, Wangb Y, Ghitab O, Sunc J. Discrete element simulation and experimental study of powder spreading process in additive manufacturing. *Powder Technol*. 2016;306:45-54.

47. Zocca A, Günster J. Towards a debinding-free additive manufacturing of ceramics: A development perspective of water-based LSD and LIS technologies. *Open Ceram*. 2024;19:100632.

    doi: 10.1016/J.OCERAM.2024.100632

48. Oropeza D, Penny RW, Gilbert D, Hart AJ. Mechanized spreading of ceramic powder layers for additive manufacturing characterized by transmission x-ray imaging: Influence of powder feedstock and spreading parameters on powder layer density. *Powder Technol*. 2022;398:117053.

    doi: 10.1016/J.POWTEC.2021.117053

49. Capozzi LC, Sivo A, Bassini E. Powder spreading and spreadability in the additive manufacturing of metallic materials: A critical review. *J Mater Process Technol*. 2022;308:117706.

    doi: 10.1016/J.JMATPROTEC.2022.117706

50. Zinatlou Ajabshir S, Sofia D, Hare C, Barletta D, Poletto M. Experimental characterisation of the spreading of polymeric powders in powder bed fusion additive manufacturing process at changing temperature conditions. *Adv Powder Technol*. 2024;35(4):104412.

    doi: 10.1016/J.APT.2024.104412

51. Haydari Z, Talebi F, Mehrabi M, *et al*. Insights into the assessment of spreadability of stainless steel powders in additive manufacturing. *Powder Technol*. 2024;439:119667.

    doi: 10.1016/J.POWTEC.2024.119667

52. Cheng M, Tang J Bin, Zhao YH, *et al*. Validation of powder layering simulation via packing density measurement for laser-based powder bed fusion. *IOP Conf Ser Mater Sci Eng*. 2023;1296(1):012020.

    doi: 10.1088/1757-899X/1296/1/012020

53. Tan P, Zhou M, Tang C, Su Y, Qi HJ, Zhou K. Multiphysics modelling of powder bed fusion for polymers. *Virtual Phys Prototyp*. 2023;18(1):e2257191.

    doi: 10.1080/17452759.2023.2257191

54. Salehi H, Cummins J, Gallino E, *et al*. Optimising spread-layer quality in powder additive manufacturing: Assessing packing fraction and segregation tendency. *Processes*. 2023;11(8):2276.

    doi: 10.3390/PR11082276

55. Li H, Elsayed H, Colombo P. Effect of particle size distribution and printing parameters on alumina ceramics prepared by Additive Manufacturing. *Ceram Int*. 2024;50(4):6340-6348.

    doi: 10.1016/J.CERAMINT.2023.11.365

56. Marinucci F, Aversa A, Manfredi D, Lombardi M, Fino P. Evaluation of a laboratory-scale gas-atomized AlSi10Mg powder and a commercial-grade counterpart for laser powder bed fusion processing. *Materials*. 2022;15(21):7565.

    doi: 10.3390/MA15217565

57. Morcos P, Shoukr D, Sundermann T, *et al*. An all-encompassing study on the joint effect of powder feedstock

characteristics and manufacturing process parameters on the densification and mechanical properties of additively manufactured nickel alloy 718. *Addit Manuf*. 2023;78:103828.

doi: 10.1016/J.ADDMA.2023.103828

58. Zhao W, Chang J, Wei Q, Wu J, Ye C. Effect of sodium silicate solution combined yttrium oxide stabilized zirconia nanopowders on the properties of alumina ceramics fabricated by binder jetting additive manufacturing. *J Mater Process Technol*. 2024;330:118454.

    doi: 10.1016/J.JMATPROTEC.2024.118454

59. Wu H, Jiang C, Tang C, *et al.* Binder jetting printed in situ mullite strengthened alumina ceramics with excellent mechanical and thermal properties through multi-phase infiltration. *Virtual Phys Prototyp.* 2024;19(1):e2427240.

    doi: 10.1080/17452759.2024.2427240

60. Manotham S, Tesavibul P. Effect of particle size on mechanical properties of alumina ceramic processed by photosensitive binder jetting with powder spattering technique. *J Eur Ceram Soc*. 2022;42(4):1608-1617.

    doi: 10.1016/J.JEURCERAMSOC.2021.11.062

61. Du W, Ren X, Chen Y, Ma C, Radovic M, Pei Z. Model guided mixing of ceramic powders with graded particle sizes in binder jetting additive manufacturing. In: *ASME 2018 13th International Manufacturing Science and Engineering Conference, MSEC 2018*; 2018. p. 1.

    doi: 10.1115/MSEC2018-6651

62. *C566 Standard Test Method for Total Evaporable Moisture Content of Aggregate by Drying*. Available from: https://store.astm.org/c0566-19.html [Last accessed on 2025 May 08].

63. Bui HM, Fischer R, Szesni N, *et al.* Development of a manufacturing process for Binder Jet 3D printed porous Al2O3 supports used in heterogeneous catalysis. *Addit Manuf*. 2022;50:102498.

    doi: 10.1016/J.ADDMA.2021.102498

64. Yu AB, Zou RP, Standish N. Modifying the linear packing model for predicting the porosity of nonspherical particle mixtures. *Ind Eng Chem Res*. 1996;35(10):3730-3741.

    doi: 10.1021/IE950616A/ASSET/IMAGES/LARGE/IE950616AF00016.JPEG

65. Juarez-Enriquez E, Olivas GI, Zamudio-Flores PB, Ortega-Rivas E, Perez-Vega S, Sepulveda DR. Effect of water content on the flowability of hygroscopic powders. *J Food Eng*. 2017;205:12-17.

    doi: 10.1016/J.JFOODENG.2017.02.024

66. Elliott AM, Nandwana P, Siddel D, Compton BG. A Method for Measuring Powder Bed Density in Binder Jet Additive Manufacturing Process and the Powder Feedstock Characteristics Influencing the Powder Bed Density. In: *International Solid Freeform Fabrication Symposium*. University of Texas at Austin; 2016. Available from: https://hdl.handle.net/2152/89652 [Last accessed on 2025 May 08].

67. Kaleem MA, Alam MZ, Khan M, Jaffery SHI, Rashid B. An experimental investigation on accuracy of Hausner Ratio and Carr Index of powders in additive manufacturing processes. *Metal Powder Report*. 2021;76:S50-S54.

    doi: 10.1016/J.MPRP.2020.06.061

68. Shah RB, Tawakkul MA, Khan MA. Comparative evaluation of flow for pharmaceutical powders and granules. *AAPS PharmSciTech*. 2008;9(1):250-258.

    doi: 10.1208/S12249-008-9046-8/FIGURES/9

69. Sandler N, Reiche K, Heinämäki J, Yliruusi J. Effect of moisture on powder flow properties of theophylline. *Pharmaceutics*. 2010;2(3):275.

    doi: 10.3390/PHARMACEUTICS2030275

70. Martins GHB, Morgado WAM, Queirós SMD, Atman APF. Large-deviation quantification of boundary conditions on the Brazil nut effect. *Phys Rev E*. 2021;103(6):062901.

    doi: 10.1103/PHYSREVE.103.062901/FIGURES/10/MEDIUM

71. He Y, Hassanpour A, Bayly AE. Linking particle properties to layer characteristics: Discrete element modelling of cohesive fine powder spreading in additive manufacturing. *Addit Manuf*. 2020;36:101685.

    doi: 10.1016/J.ADDMA.2020.101685

72. Xu R, Nan W. Analysis of the metrics and mechanism of powder spreadability in powder-based additive manufacturing. *Addit Manuf*. 2023;71:103596.

    doi: 10.1016/J.ADDMA.2023.103596

73. Toth JR, Phillips AK, Rajupet S, Sankaran RM, Lacks DJ. Particle-size-dependent triboelectric charging in single-component granular materials: Role of humidity. *Ind Eng Chem Res*. 2017;56(35):9839-9845.

    doi: 10.1021/ACS.IECR.7B02328/ASSET/IMAGES/LARGE/IE-2017-023286_0004.JPEG

74. Wu Y, Fan Z, Lu Y. Bulk and interior packing densities of random close packing of hard spheres. *J Mater Sci*. 2003;38(9):2019-2025.

    doi: 10.1023/A:1023597707363/METRICS

75. Wu Y, An X, Huang F. DEM simulation on packing densification of equal spheres under compression. *Mater Res Innov*. 2014;18:S41082-S41086.

    doi: 10.1179/1432891714Z.000000000825

76. Zhou J, Zhang Y, Chen JK. Numerical simulation of random packing of spherical particles for powder-based additive manufacturing. *J Manuf Sci Eng*. 2009;131(3):0310041-0310048.

    doi: 10.1115/1.3123324/470682

77. Li M, Miao G, Du W, Pei Z, Ma C. Difference between powder bed density and green density for a free-flowing powder in binder jetting additive manufacturing. *J Manuf Process*. 2022;84:448-456.

    doi: 10.1016/J.JMAPRO.2022.10.030

78. Huang X, Lang L, Wang G, Alexandrov S. Effect of powder size on microstructure and mechanical properties of 2A12Al compacts fabricated by hot isostatic pressing. *Adv Mater Sci Eng*. 2018;2018(1):1989754.

    doi: 10.1155/2018/1989754

79. Du W, Roa J, Hong J, Liu Y, Pei Z, Ma C. Binder jetting additive manufacturing: Effect of particle size distribution on density. *J Manuf Sci Eng Trans ASME*. 2021;143(9):091002.

    doi: 10.1115/1.4050306/1100582

80. Yim S, Bian H, Aoyagi K, Yamanaka K, Chiba A. Spreading behavior of Ti48Al2Cr2Nb powders in powder bed fusion additive manufacturing process: Experimental and discrete element method study. *Addit Manuf*. 2022;49:102489.

    doi: 10.1016/J.ADDMA.2021.102489

81. Mariani M, Beltrami R, Brusa P, Galassi C, Ardito R, Lecis N. 3D printing of fine alumina powders by binder jetting. *J Eur Ceram Soc*. 2021;41(10):5307-5315.

    doi: 10.1016/j.jeurceramsoc.2021.04.006

82. Rahman KM, Miyanaji H, Williams CB. Effects of binder droplet size and powder particle size on binder jetting part properties. *Rapid Prototyp J*. 2023;29(8):1715-1729.

    doi: 10.1108/RPJ-10-2022-0358/FULL/XML